Journal of Materials Chemistry A

ROYAL SOCIETY OF CHEMISTRY

PAPER

View Article Online
View Journal | View Issue



Cite this: J. Mater. Chem. A, 2025, 13, 31642

# Long-term stability of GaN-based photocatalyst nanostructures through dynamic oxide protection†

Ishtiaque Ahmed Navid, Zhengwei Ye, Yuyang Pan, Yifan Shen, Theodore Norris and Zetian Mi*

Solar photocatalytic reactions are a very promising approach to clean energy production. Even though significant efficiency improvement has been made in photocatalytic devices, simultaneously achieving their long-term stability has remained a formidable challenge. As such, to date, there have been very few demonstrations of semiconductor photocatalysts showing stable and long-term operation under concentrated solar irradiation, crucial for practical applications. Herein, we design a unique photocatalyst protection architecture comprising an $Al_2O_3$ capping layer on the cocatalyst-decorated light-absorbing GaN-based nanostructures to mitigate two of the most dominant bottlenecks in long-term stability: photocatalytic corrosion and cocatalyst nanoparticle displacement. Thereby, we demonstrate the stable operation of this oxide-protected photocatalyst nanostructure for ~1500 hours without significant performance degradation under concentrated sunlight, which is significantly longer than the stability of the photocatalyst without any protection. Detailed investigation reveals the dynamic characteristic of the capping layer, where Al atoms diffuse from the nanowire *c*-plane toward the *m*-plane during the reaction and subsequently get oxidized to form an $Al_2O_3$ layer. As such, this protection architecture stabilizes the cocatalyst nanoparticles on the sidewall *m*-plane and prevents the photocatalyst top *c*-plane corrosion at the same time. Our study overcomes the critical challenge of simultaneously achieving high efficiency and stability in clean fuel generation, offering a crucial means for practical applications of photocatalytic devices for sustainable green energy.

Received 8th April 2025
Accepted 15th July 2025

DOI: 10.1039/d5ta02771c

rsc.li/materials-a



## Introduction

Hydrogen production through solar water splitting is a very promising approach for solar energy conversion to chemical fuels.[1,2] Along this line, unassisted photocatalytic solar water splitting at a stoichiometric $H_2$ to $O_2$ ratio of 2 : 1 is crucial for sustainable and renewable green fuel production.[3–5] The counter electrode is deposited on the surface of the photocatalyst as nanoparticle cocatalysts in this wireless counterpart of the photoelectrochemical water splitting process,[6–9] which can substantially reduce the system cost due to its simplicity. Furthermore, photocatalytic solar water splitting can viably operate in freshwater or seawater[2,10] with no additional bias or circuitry and can thus address the important photocatalytic stability and safety-related concerns.[3,11,12] Despite the substantial improvement in the solar-to-hydrogen (STH) conversion efficiency of the photocatalytic devices,[13–20] their long-term stability has remained a considerable challenge, which has thus far prevented their practical large-scale applications.

Some of the most critical issues limiting the long-term stability of photocatalytic reactions are primarily photocatalytic corrosion and cocatalyst nanoparticle displacement (*i.e.*, agglomeration and detachment) as depicted schematically in Fig. 1a. Catalytic corrosion is a common phenomenon for any materials reacting in aqueous media, leading to their faster deactivation.[21–24] Furthermore, the photocatalytic activity is directly correlated to the uniformity of cocatalyst nanoparticle dispersion on the photocatalyst surface.[25,26] These nanoparticles tend to migrate and aggregate on the photocatalyst surface in response to thermal or optical excitation due to the formation energy difference resulting from the lattice mismatch variation between the nanoparticles and different photocatalyst facets.[27] The resulting nanoparticle agglomeration leads to the degradation of photocatalytic activity because of the reduced number of active sites on the semiconductor material surface.[28–34] Moreover, cocatalyst nanoparticle detachment or dissolution during the reaction can also result in the loss of active sites,[35–37] leading to an expedited deactivation of the photocatalyst materials. Therefore, addressing these major limiting factors for photocatalytic stability will play a vital role in achieving enhanced longevity of the photocatalyst material.

III-nitride semiconductors such as InGaN are one of the few materials among the currently known photocatalysts[38] with

*Department of Electrical Engineering and Computer Science, University of Michigan, Ann Arbor, 1301 Beal Avenue, Ann Arbor, MI 48109, USA. E-mail: ztmi@umich.edu*

† Electronic supplementary information (ESI) available. See DOI: https://doi.org/10.1039/d5ta02771c

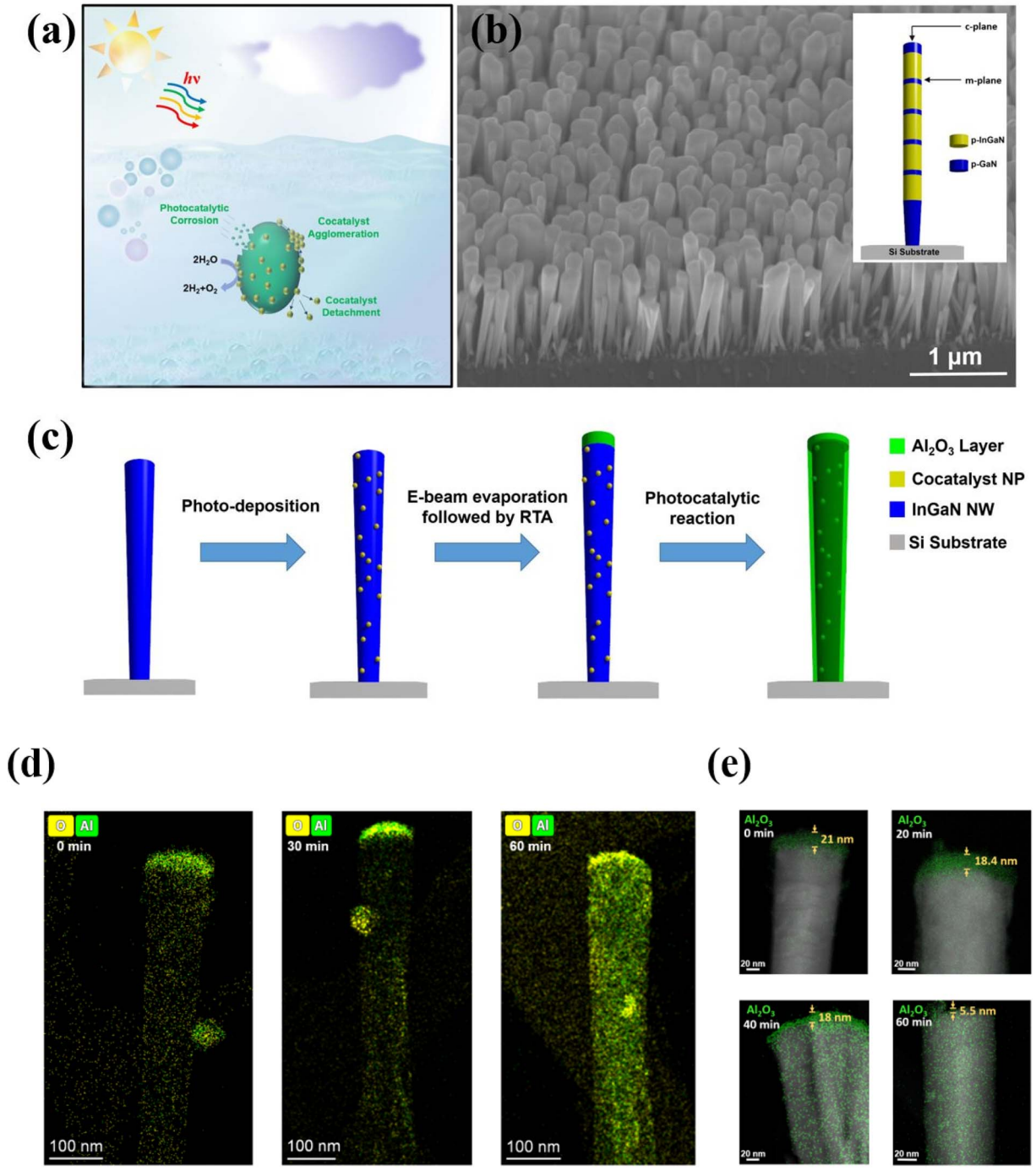


Fig. 1 (a) Schematic illustration of photocatalytic corrosion and cocatalyst nanoparticle displacement during the reaction. (b) 45° tilt SEM image of the as-grown p-InGaN nanowire (NW) array. The schematic of the different layers of the p-InGaN nanowire photocatalyst is shown in the inset. (c) Preparation flow of the $Al_2O_3$-protected p-InGaN nanowire sample with cocatalyst nanoparticles (NPs). (d) EDX elemental mapping of the $Al_2O_3$-capped cocatalyst-decorated p-InGaN nanowires after 0 min, 30 min, and 60 min of photocatalytic reactions. (e) HAADF-STEM-EDX mapping of the nanowire showing the $Al_2O_3$ thickness change after 0 min, 20 min, 40 min, and 60 min of photocatalytic reactions.

a tunable energy band gap across the solar spectrum while straddling the water redox potentials under the irradiation of ultraviolet (UV) and visible light.[39–42] As such, these semiconductor materials are very promising as efficient light absorbers for enhanced photocatalytic activity in solar water splitting. Moreover, the considerable chemical stability of metal–nitride semiconductors makes them a viable option as photocatalysts for practical solar water splitting applications.[43,44] Furthermore, the inclusion of protection layers has been reported to significantly enhance the stability of different photoelectrodes for PEC solar water splitting.[45–49] On the other hand, Lyu *et al.*[35] showed that the photo-deposition of CoOOH

and $TiO_2$ on oxide-based photocatalysts helped reduce the cocatalyst dissolution and significantly enhanced the material durability. The work of Han *et al.*[50] also reported improved stability of oxide photocatalysts resulting from $CrO_x$ modification.

In this work, we have investigated the major challenges associated with realizing the long-term stability of the InGaN nanowire-based photocatalyst. Detailed studies show that the nanowire structure is severely affected by photocatalytic etching at the top *c*-plane, cocatalyst nanoparticle aggregation along the lateral *m*-plane surfaces, and the loss of cocatalyst nanoparticles over time. Thereby, we design a dynamic protection scheme comprising an $Al_2O_3$ capping layer on the nanowire photocatalyst structure, and this architecture demonstrates a significant enhancement in the photocatalytic longevity. The $Al_2O_3$ protection layer evolves during the reaction by getting partly redistributed from the nanowire *c*-plane toward the nonpolar sidewall. This, in turn, not only facilitates the prevention of nanowire etching and nanoparticle aggregation at the *c*-plane but also inhibits the detachment of the nanoparticles by stabilizing them on the *m*-plane. Such a unique protection architecture can eventually help realize the implementation of long-term stable photocatalyst devices for large-scale sunlight-driven overall water splitting.

## Results and discussion

The scanning electron microscopy (SEM) image of the as-grown p-InGaN/GaN nanowire sample on the Si (111) substrate synthesized with molecular beam epitaxy is shown in Fig. 1b. The schematic illustration showing the different layers of the nanowire structure is depicted in the inset. The details of the epitaxial growth can be found in our previous studies.[37,51] The length of the nanowires is ~850 nm with a diameter of ~150 nm. $Rh/Cr_2O_3$ core/shell and $CoO_x$ nanoparticles were photo-deposited on the p-type InGaN/GaN nanowires as the cocatalysts to promote $H_2$ and $O_2$ generation, respectively.[52–56] Fig. 1c demonstrates the steps involved in synthesizing the $Al_2O_3$-protected InGaN nanowire photocatalyst. Here, a thin (~20 nm) protective $Al/Al_2O_3$ capping layer on top of the cocatalyst decorated p-InGaN nanowire has been designed in order to suppress the severe nanowire etching and cocatalyst nanoparticle displacement. For this protection design, an Al capping layer was deposited with electron-beam (e-beam) evaporation. Subsequently, rapid thermal annealing (RTA) in the $O_2$ environment at 500 °C for 5 min was performed. In this preparation process, some portion of the deposited Al will get oxidized to form a partially $Al_2O_3$-coated Al layer. Apart from primarily protecting the top *c*-plane of the nanowire photocatalyst, this design does not block the catalytically active sites on the *m*-plane,[57] due to the directional nature of the e-beam deposition. $O_2$ treatment is also reported to catalytically further stabilize the material.[58,59] As such, this protection scheme will help increase the longevity of the photocatalyst without sacrificing its activity. Upon conducting photocatalytic reactions on this structure, the dynamic nature of the oxide layer can be observed as the Al atoms of the capping layer deposited on the nanowire tip migrate to the sidewall *m*-plane and subsequently get oxidized as depicted in the final step of Fig. 1c.

The scanning transmission electron microscopy (STEM) along with the elemental mapping in Fig. 1d confirms the successful e-beam deposition of Al followed by the $O_2$ environment RTA, forming a thin $Al_2O_3$-coated Al layer on top of the nanowire structure before the reaction. As can be observed in the STEM with chemical mappings of the structure with different reaction durations in Fig. 1d, the $Al/Al_2O_3$ capping layer stays on the nanowire tip at the initial stage of the reaction without undergoing much change. However, the $Al/Al_2O_3$ protection layer starts changing and gets redistributed after 60 min of the photocatalytic reaction. With the ongoing reaction, the $Al/Al_2O_3$ capping layer continues to absorb optical excitation from the light source, and this will result in the localized heating of Al metal species.[60] Consequently, there will be a thermal gradient from the photocatalyst nanowire tip towards the bottom with the heated side on top. As such, a thermal migration force will be applied on the Al adatoms in the direction opposite to the thermal gradient and, therefore, the Al adatoms will diffuse from the heated nanowire tip towards the relatively cold nanowire sidewall and root.[61–63] These thermally migrated Al atoms eventually get oxidized during the photocatalytic reaction to form $Al_2O_3$ on the nanowire sidewall. In this experiment, it takes ~60 min for the capping layer Al atoms to acquire sufficient thermal energy from the optical excitation to overcome the diffusion energy barrier for the thermal migration,[61] which is reflected by the significant capping layer redistribution after 60 min Fig. 1e depicts the high-angle annular dark field (HAADF)-STEM elemental mappings of the nanostructure showing the thickness change of the $Al/Al_2O_3$ capping layer over time. It can be observed that the decrease in the $Al/Al_2O_3$ top layer thickness is considerably small for the first 40 min of the reaction, even though the $Al_2O_3$ formation on the sidewall starts becoming noticeable after 40 min. However, after 60 min of the reaction, the $Al_2O_3$ top layer thickness is significantly reduced with much more enhanced oxide layer attachment on the sidewall.

As such, more detailed experiments were performed for understanding the dynamic nature of the $Al_2O_3$ protection layer on the InGaN photocatalyst. In order to further elucidate this phenomenon, X-ray photoelectron spectrum (XPS) measurements were done on these samples where the *c*-plane nanowire surfaces were predominantly measured, and the results are shown in ESI Fig. S1.† The XPS signal for the Al 2p orbital is initially strong on the top *c*-plane of the nanowire. Based on the STEM elemental mapping before reaction shown in Fig. 1d, the estimated Al amount is ~51 at% whereas the O amount is ~48 at%. The substoichiometric O amount indicates the presence of Al and $Al_2O_3$ in this capping layer at the initial stage. After a longer reaction time, the Al 2p signal strength considerably decreases due to the Al redistribution from the *c*-plane. Moreover, as can be seen in the STEM with Al mapping in ESI Fig. S2,† the Al in the *c*-plane capping layer migrates to the nanowire sidewall during the initial stage of the reaction (60 min). As the reaction continues, some portion of this Al gets

 

oxidized to stay on the sidewall while the rest starts to dissolve in the water solution. For the longer durations of the photocatalytic reaction (1–64 days), the Al signal intensity in the STEM elemental mapping becomes much weaker, which indicates that more Al from the nanowire sidewall continues to dissolve in water with the ongoing long-term reaction. This is further corroborated by the inductively coupled plasma-atomic emission spectrometer (ICP-AES) test shown in ESI Fig. S3.† It can be observed that the total Al content dissolved in water continues to increase as the long-term reaction goes on. Furthermore, the high resolution (HR)-STEM image shown in ESI Fig. S4a† indicates that there is no formation of $Al/Al_2O_3$ lattices within the metal cocatalyst nanoparticles during the reaction. The nanoparticles mainly contain the lattices of Rh/Cr/Co oxides. Furthermore, the HR-HAADF-STEM-EDX mapping of the nanowire showing the Al distribution after ~300 hours of reaction is depicted in ESI Fig. S4b.†

Subsequently, photocatalytic stability experiments for overall water splitting (OWS) have been performed in pure water at 70 °C (ref. 37) temperature under concentrated simulated solar illumination (10 suns or 1000 mW $cm^{-2}$). Previous studies in the literature report that increased light intensity results in faster photocatalytic degradation.[64,65] Our experiments indicate a proportional reduction in photocatalytic stability with increasing light intensity. For the same cocatalyst-decorated, unprotected InGaN nanowire samples with the same light source, our earlier research reported approximately 78 hours of photocatalytic stability with 30 suns,[37] while this study observed around 240 hours of stability with 10 suns (ESI Fig. S5†). Hence, we have used the same light intensity (10 suns) for all the photocatalytic long-term stability experiments in this work for consistency. The stability results for the samples with different $Al/Al_2O_3$ capping layer thicknesses (5 nm, 10 nm, and 20 nm) are displayed in Fig. 2a. It is noticeable that the stability of the structure increases with thicker oxide protection layers. If the capping layer is thin, there will not be enough Al atoms that can migrate and subsequently get oxidized to cover the nanowire sidewall entirely. As such, there will be exposed portions of the nanowire sidewall with no oxide protection, resulting in worse photocatalytic stability for samples with sub-optimal capping layer thickness. The periodic fluctuations observed in stability data can be primarily caused by two factors: (1) test error from measurement variation, and (2) dynamic reconstruction of the photocatalyst. Test error due to measurement variation is possible, as each cycle of measurement is done manually at separate times. For each cycle of measurement, the reaction chamber was pumped down to a vacuum before the water splitting reaction. Then, the photocatalytic reaction was performed, and the hydrogen and oxygen gases produced were sampled with a vacuum-tight syringe. Subsequently, the gas samples were analyzed in a Shimadzu GC-8A gas chromatography machine. The fluctuation can result from several cycles of such measurements. Furthermore, the dynamic reconstruction of the photocatalyst material is also common during the reaction.[66,67] Specifically, the photocatalyst surface structure may not be constant during the long-term photocatalytic reaction, which often experiences periodic reconstruction. This phenomenon can also contribute to the STH data fluctuation.

Moreover, the STH conversion efficiency of the photocatalyst nanowires in this protection design is not adversely affected. This is because the oxide protection architecture does not create any physical barrier between the nanowire sidewall-anchored active sites and the aqueous solution. This has been further corroborated by conformal deposition of an ~0.5 nm thick $Al_2O_3$ layer *via* atomic layer deposition (ALD) on the photocatalyst nanowire sample and testing its water splitting activity.

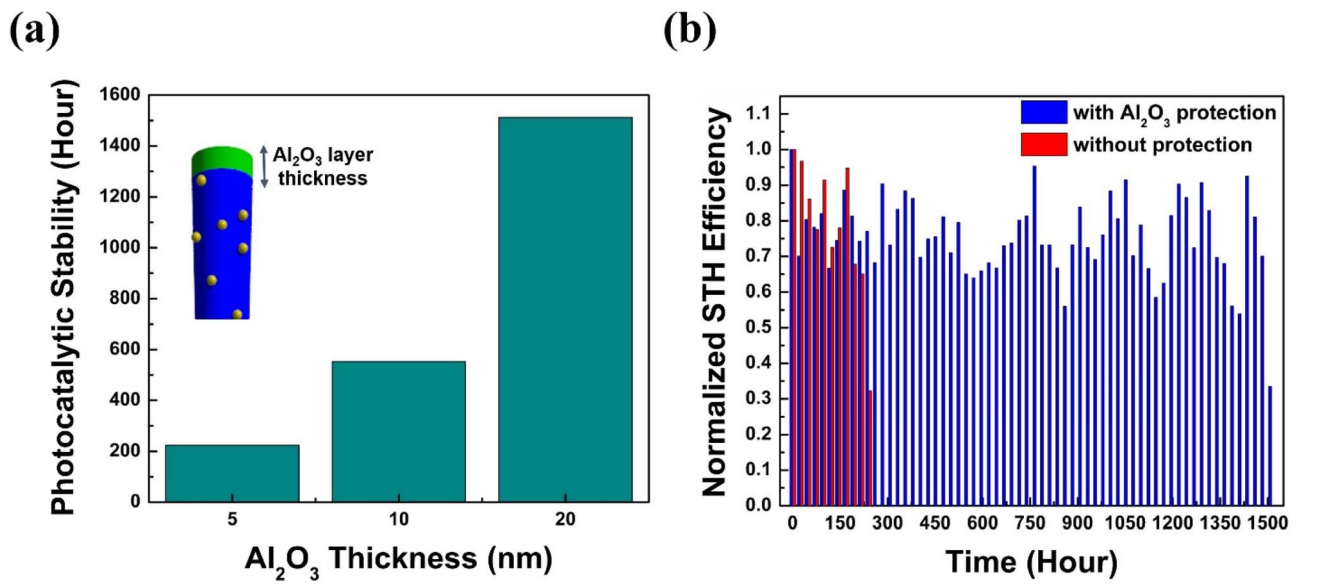


Fig. 2 (a) Photocatalytic stability of the $Al_2O_3$-capped cocatalyst-loaded p-InGaN nanowire samples with different $Al_2O_3$ capping thicknesses. (b) Stability test of the cocatalyst-decorated p-InGaN nanowires with and without $Al_2O_3$-capping under concentrated light of 1000 mW $cm^{-2}$ at 70 °C temperature.

As can be seen in ESI Fig. S6,† even such a thin $Al_2O_3$ layer deposited by conformal ALD significantly reduces the STH efficiency of the nanowire photocatalyst since it essentially blocks the active sites on the nanowire *m*-plane. Furthermore, the photocatalytic test result over time with normalized STH efficiency for cocatalyst-loaded samples with a 20 nm Al/$Al_2O_3$ capping layer and without protection is shown in Fig. 2b. Here, it can be observed that the cocatalyst-decorated p-type InGaN nanowire photocatalyst without any protection layer can retain more than 50% of its maximum activity for approximately 250 hours before it gets deactivated (<50% of the maximum activity value). On the other hand, remarkably enhanced photocatalytic stability has been achieved in the $Al_2O_3$-protected architecture where it has been able to sustain more than 50% of its maximum activity for ~1500 hours (as compared to ~250 hours for the sample without any protection layer). The stability test results with 5 nm and 10 nm Al/$Al_2O_3$ layer thicknesses are displayed in ESI Fig. S7.† Moreover, the SEM images shown in ESI Fig. S8a and b† respectively demonstrate that, without $Al_2O_3$ protection, the etching and the cocatalyst nanoparticle agglomeration take place on the top *c*-plane of the nanowires after the reaction.

To investigate the cocatalyst displacement phenomenon in detail, STEM elemental mapping has been performed on both the unprotected and $Al_2O_3$-protected samples after several hours of reaction, as shown in Fig. 3a and b. There is a clear agglomeration of the cocatalyst nanoparticles observed for the sample with no $Al_2O_3$ protection after several hours of photocatalytic reaction (Fig. 3a). Furthermore, the EDX spectra in ESI Fig. S9† also demonstrate the agglomeration of the cocatalyst nanoparticles (Cr, Co, and Rh) in the unprotected nanowires after several hours of photocatalytic reaction, mostly towards the top *c*-plane. Previous studies report that the hydrogen bubble growth induces mechanical stress on the cocatalyst nanoparticle surface. This stress drives the cocatalyst nanoparticle migration and agglomeration towards nanowire facets with different formation energies, resulting in severe degradation of the photocatalytic performance.[68] On the other hand, the cocatalyst nanoparticles did not undergo much agglomeration for the $Al_2O_3$-protected sample even after ~200 hours of reaction as shown in Fig. 4b. As mentioned earlier, the Al/$Al_2O_3$

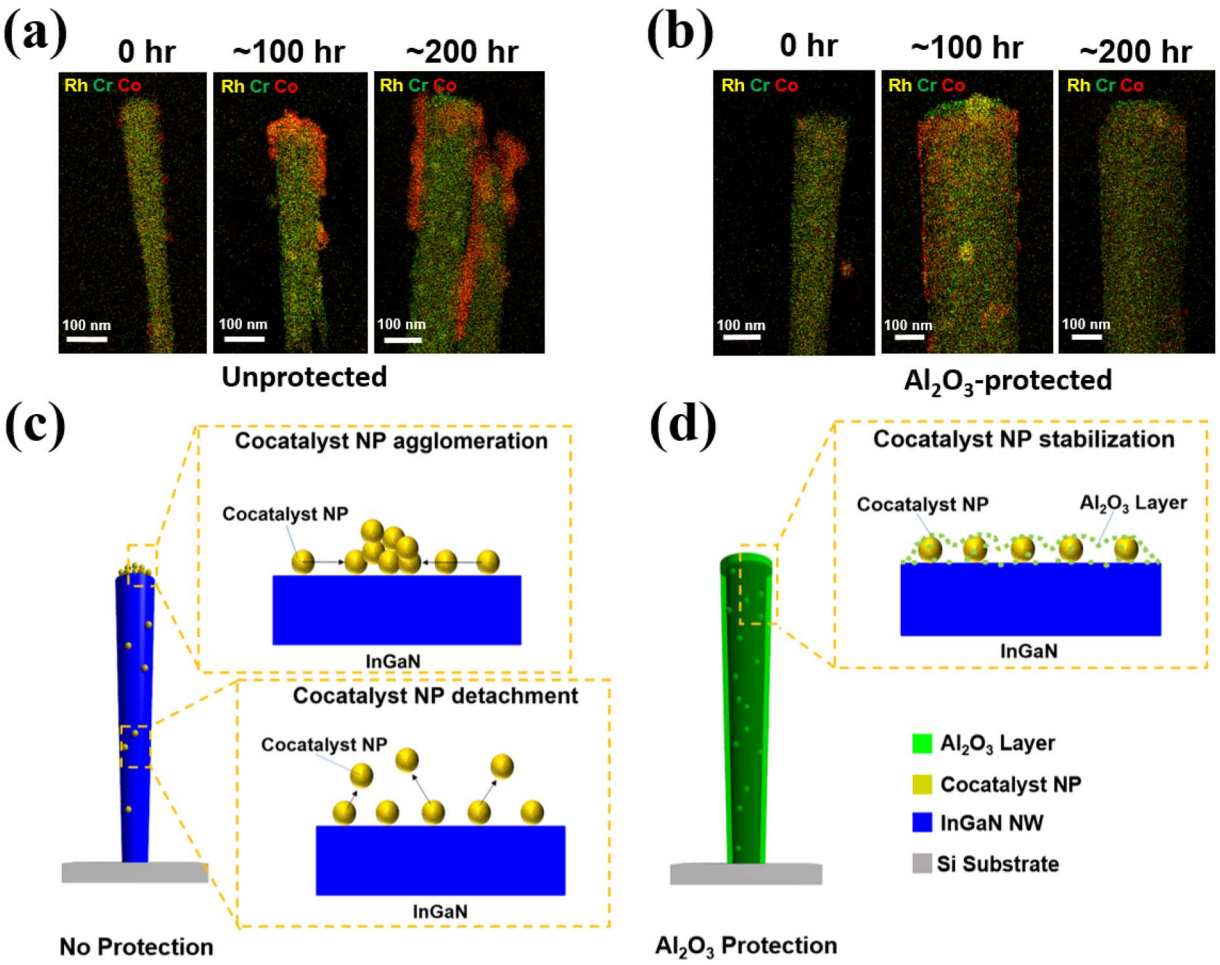


Fig. 3 EDX elemental mappings of the cocatalyst-loaded samples for different reaction durations (a) without and (b) with $Al_2O_3$ protection. The cocatalyst NPs are agglomerated in the case of no $Al_2O_3$ protection. Schematic depictions of the (c) cocatalyst NP displacement in the unprotected nanostructure and (d) cocatalyst stabilization effect by the $Al_2O_3$ protection layer.

 

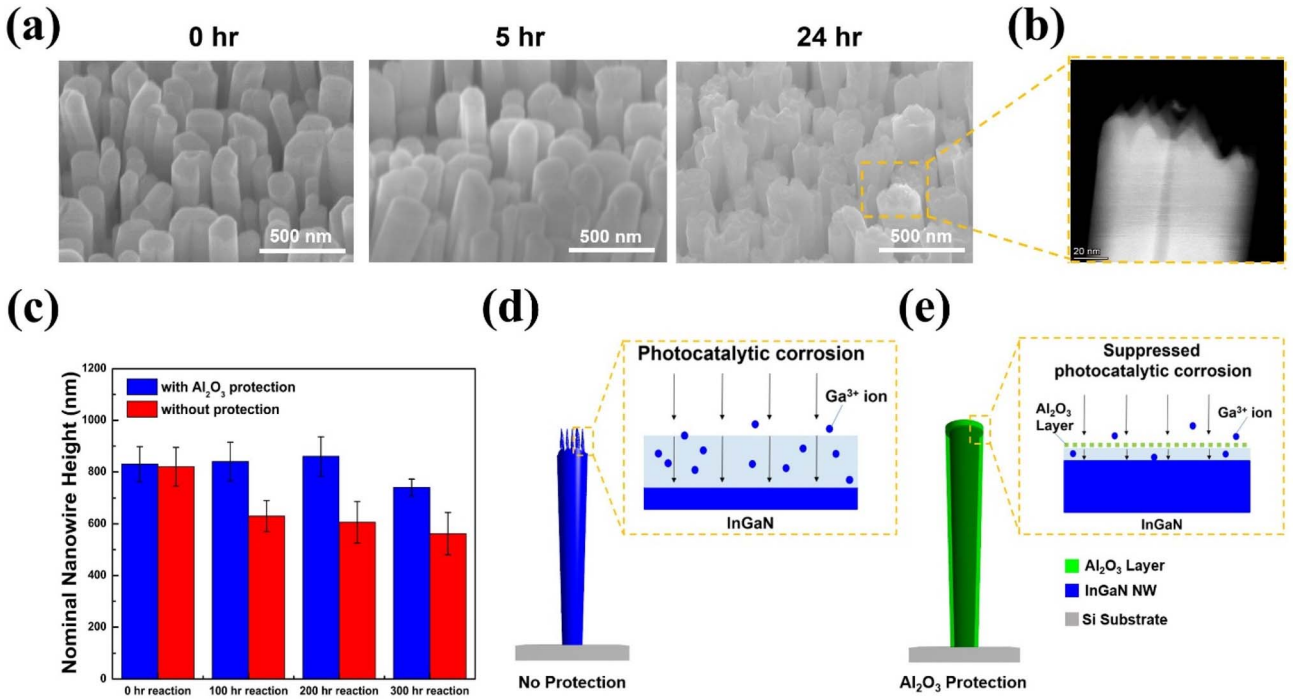


Fig. 4 (a) 45° tilt SEM images depicting the time evolution of the undecorated unprotected p-InGaN nanowire structure during a 24-hour photocatalytic reaction. (b) Magnified HAADF-STEM of the etched p-InGaN nanowires from the yellow-boxed region in the nanowire structure of (a). (c) Nominal nanowire height of the cocatalyst-decorated sample with and without $Al_2O_3$ protection for different reaction durations. Schematic illustration of the (d) photocatalytic corrosion in the unprotected nanostructure and (e) reduced corrosion due to the $Al_2O_3$ protection.

protection layer initially covers the top *c*-plane, and Al subsequently redistributes itself to the sidewall *m*-plane of the nanowire followed by oxidation during the photocatalytic reaction. Thus, the $Al_2O_3$ layer occupies different photocatalyst facets, primarily the nanowire top *c*-plane and sidewall *m*-plane. As previously discussed, these different nanowire facets have different formation energies, and this variation in the formation energy causes the nanoparticles to migrate and aggregate from one photocatalyst surface to another in response to optical or thermal excitation. As such, the $Al_2O_3$ coverage on different surfaces all over the nanowire will minimize the variation in the formation energies of different photocatalyst facets, and this, in turn, results in suppressed cocatalyst migration and agglomeration.

Furthermore, an ICP-AES test was conducted to compare the cocatalyst (Rh, Cr, Co) amount in water after the long-term reactions for the samples with and without $Al_2O_3$ protection (ESI Fig. S10†). It can be observed that the amount of dissolved cocatalyst nanoparticles in water is reduced for the $Al_2O_3$-protected sample compared to the one without protection, suggesting the reduced cocatalyst detachment for the oxide-coated sample. Usually, the metal nanoparticles on Ga(In)N nanowires are either physically adsorbed on the nanowire surface or there is a lattice alignment between metal nanoparticles and Ga(In)N nanowires. The lattice-matched metal nanoparticles have a strong binding at the nanoparticle–nanowire interface, and this helps anchor the nanoparticle cocatalysts on the photocatalyst nanowire surface even under harsh reaction conditions.[69] However, the surface-adsorbed metal nanoparticles have much weaker bonding strength at the nanoparticle–nanowire interface, and as such, they are more susceptible to mechanical detachment. In the case of the $Al_2O_3$-protected sample, Al atoms migrate to different photocatalyst sites[63,70] at the metal nanoparticle–Ga(In)N nanowire interface (ESI Fig. S4b†) as the reaction happens. Some portion of this redistributed Al that gets oxidized will reside at the interface between the weakly bonded surface-adsorbed metal nanoparticles and Ga(In)N nanowire. With the presence of $Al_2O_3$ in these weakly bonded interfacial regions, the cocatalyst metal atoms will be trapped on the surface $O^{2-}$ sites, which results in the increased activation energy of metal nanoparticle detachment from the $O^{2-}$ modified photocatalyst surface.[71,72] Furthermore, $Al_2O_3$ as a support is reported to possess relatively robust metal–support interaction strength for a given metal due to its high Hüttig and Tamman temperatures.[73,74] Consequently, there is reduced dissociation of the metal species from the oxide surface and they are anchored on $Al_2O_3$ by chemical bonds formed through an atom-trapping mechanism.[75,76] This leads to the further stabilization of the nanoparticle–nanowire binding strength in these relatively susceptible regions and reduces the cocatalyst detachment from the oxide-protected photocatalyst surface. Here, it can be observed from ESI Fig. S10† that there is initial Cr dissolution in the long-term photocatalytic reaction for both the $Al_2O_3$-protected and unprotected samples. This

could be due to the accelerated dissolution of Cr through the formation of $CrOH^{2+}$ and $Cr(OH)_3$ (ref. 77) in the solution at the early stage of the photocatalytic reaction. However, the amount of Cr dissolution in the long-term reaction (5 days or longer) is much more suppressed in the $Al_2O_3$-protected samples than that of the unprotected samples due to the stabilization effect of the oxide-protected surface, as explained earlier, resulting in the overall better long-term photocatalytic stability. On the other hand, the change of Co amount over time shown here is below the detection limit of the measurement. The overall cocatalyst displacement phenomenon, including agglomeration and detachment in the unprotected photocatalyst has been schematically illustrated in Fig. 3c. The nanoparticle stabilization on the photocatalyst surface resulting from the oxide protection architecture is depicted by the schematic diagram in Fig. 3d.

Moreover, there are directly exposed portions of Ga(In)N photocatalysts to water where the surface charge transfer towards the water splitting reaction is slow. As such, the accumulated holes can instead oxidize the Ga(In)N surface, resulting in its dissolution into the surrounding water in the form of $Ga_2O_3$ ($Ga^{3+}$ ions).[78] In order to delve into this issue, a control photocatalytic experiment was carried out using the same reaction conditions as before on an undecorated as-grown nanowire sample. The SEM and HAADF-STEM images in Fig. 4a and b show that the undecorated sample is severely corroded on the *c*-plane within just 24 hours. Additional HAADF-STEM images for this experiment are shown in ESI Fig. S11.† This phenomenon substantiates the fact that the nanowire photocatalyst without any nanoparticle coverage or protection layer is highly susceptible to catalytic corrosion, leading to much faster deactivation. The nominal nanowire heights of the cocatalyst-loaded samples with and without $Al_2O_3$ protection for different reaction durations are shown in Fig. 4c. For ~100 hours of reaction of the sample without any protection, a significant nominal nanowire height reduction of ~200 nm is observed due to nanowire photo-corrosion compared to the samples before the reaction. The nanowire height further decreased after ~300 hours of reaction for the unprotected sample. On the other hand, there was very little to no Ga(In)N dissolution even after ~200 hours of reaction for the sample with $Al_2O_3$ protection. There was ~100 nm of nanowire height reduction after ~300 hours of reaction for this $Al_2O_3$-protected sample. The corresponding SEM image data are provided in ESI Fig. S12–S15.† The nanowire height SEM data for the as-grown sample are depicted in ESI Fig. S16a.† Moreover, the nanowire height for the $Al_2O_3$-protected sample after a ~1500-hour reaction is depicted in the SEM data of ESI Fig. S16b.† As can be observed from these data, there was no noticeable nanowire height reduction due to corrosion from ~300-hour reaction to ~1500-hour reaction. This further confirms that the $Al_2O_3$ protection layer substantially mitigates oxidative corrosion during the long-term photocatalytic reaction compared to the case of unprotected and exposed nanowire samples. Here, during the first ~300 hours of the reaction, the oxidation of the tip Al layer might be incomplete, resulting in a relatively less robust $Al_2O_3$ protection, and, therefore, nanowire height reduction to some extent is observed. Afterwards, the completely oxidized and stable $Al_2O_3$ is formed on the nanowire top plane in the long-term reaction and it prevents any further corrosion by providing a robust physical oxide barrier. The fast nanowire etching for the sample with no protection can be attributed to the cocatalyst displacement and the subsequent dissolution of the exposed portions of the photocatalyst as illustrated in the schematic of Fig. 4d. Moreover, ESI Fig. S17† displays the HAADF-STEM images with energy-dispersive X-ray (EDX) elemental mapping of a deactivated nanowire after reaction. It is noticeable that the photocatalytic corrosion took place mostly on the *c*-plane of the sample during the reaction. In contrast, the cocatalyst stabilization effect along with a physical barrier provided by the $Al_2O_3$ layer minimizes the direct exposure of the Ga(In)N photocatalyst to water. This, in turn, substantially reduces the photocatalytic corrosion of the nanowires during the reaction as schematically shown in Fig. 4e.

Time-resolved photoluminescence (TRPL) measurements are carried out to investigate the influence of catalytic corrosion and nanoparticle agglomeration on the carrier dynamics of the nanowires. The abundance of surface trap states induces Fermi level pinning on the sidewall of the nanowire and therefore downward band bending in the p-type InGaN/GaN nanowire. Under the electric field caused by downward band bending, the photo-excited carriers experience separation, leading to electron accumulation (hole depletion) near the surface region.[79] Such a separation process occurs in tens of ps, much faster than radiative recombination. Therefore, it can be recorded by the TRPL signal, which is affected by the spatial overlap of carrier distribution.[80]

Three sets of samples after 0, 2, 4, and 10 days of reaction are under measurement for comparison as shown in Fig. 5; the detailed fitting parameters for the TRPL data are shown in ESI Table S1.† Al/$Al_2O_3$-capped cocatalyst-decorated samples, which have minor catalytic corrosion and nanoparticle agglomeration, show similar PL decay curves for different reaction days (Fig. 5a). The bare InGaN nanowire samples, which experience severe catalytic corrosion primarily on the top *c*-plane but are free of nanoparticle agglomeration, don't show an apparent variation in PL decay curves with reaction days either (Fig. 5b). The rapid PL decay in these two cases shows an efficient carrier separation inside the nanowire.[81] Meanwhile, it also indicates that catalytic corrosion on the nanowire *c*-plane is not an important factor affecting the carrier dynamics inside the nanowire. In contrast, the unprotected cocatalyst-decorated samples, which suffer from catalytic corrosion and nanoparticle agglomeration simultaneously, exhibit a prolonged PL decay time with increasing reaction days (Fig. 5c). The nanoparticle migration and agglomeration change the coating thickness unevenly on the sidewall of the nanowire and form a thick coating on the upper side of the nanowire, which significantly affects the band bending of the nanowire. A thicker coating on the nanowire generally causes the surface band bending of the nanowire to align with the intrinsic band bending of the coating material.[82] The metal cocatalyst nanoparticles, which contain numerous free electrons, maintain a constant Fermi level throughout. The metallic coating reduces

 

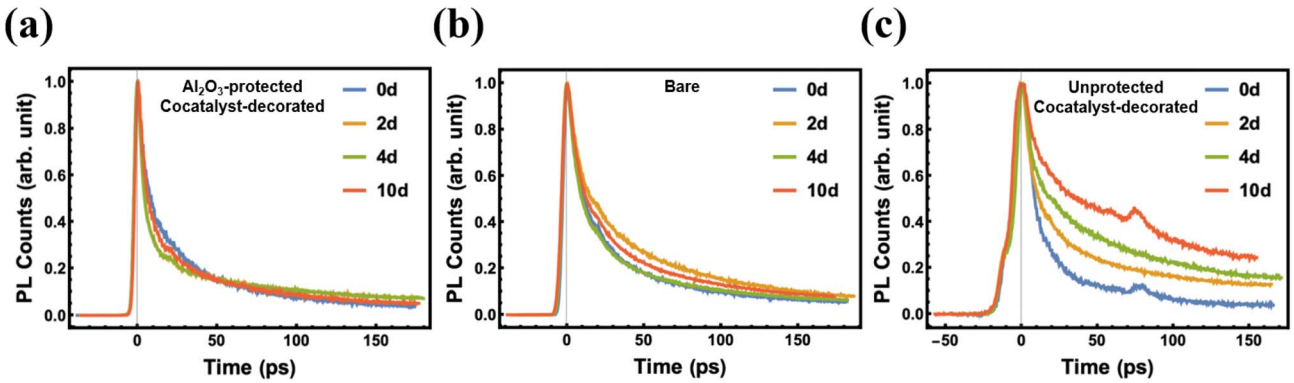


Fig. 5 TRPL signals (440–460 nm) of three sets of InGaN/GaN nanowire samples for 0, 2, 4, and 10 reaction days: (a) $Al_2O_3$-capped cocatalyst-decorated nanowire samples. (b) Bare InGaN/GaN nanowire samples with no protection and decoration. (c) Unprotected cocatalyst-decorated nanowire samples.

Fermi-level pinning on the surface of nanowires, thereby diminishing the extent of band bending. Therefore, the degree of carrier separation is reduced, which extends the decay time.[83] The TRPL data not only provide insight into the carrier dynamics during the catalyst reaction but also offer a potential nondestructive detection method for monitoring nanoparticle agglomeration and catalyst reaction efficiency after proper calibration.

Conventional surface protection by physical coating such as ALD films involves overcoating the metal nanoparticle-decorated photocatalyst nanostructure. Such coating layers preferentially decorate the low-coordinated metal sites and spatially confine or stabilize the cocatalyst nanoparticles.[84,85] As such, the nonporous ALD protection conformally coats all the photocatalyst nanostructure facets, and physically blocks the catalytically active sites of the nanostructure (*i.e.*, *m*-plane of a nanowire structure), causing catalytic efficiency degradation as seen in our experiments. A similar phenomenon was also observed in a study conducted by Alba-Rubio *et al.*[86] However, there are studies reporting the formation of a porous ALD configuration upon high-temperature calcination, which was effective in enhancing both the catalytic activity and stability.[87,88] On the other hand, the dynamic $Al_2O_3$ protection scheme involves atom trapping in stabilizing the cocatalyst metal nanoparticles on the photocatalyst surface, as explained earlier.

For context and better clarity, we further look at the stability metric comparison of the conventional ALD $Al_2O_3$ protection and dynamic $Al_2O_3$ protection. Corrosion rate of the photocatalyst and the cocatalyst detachment/leaching can be considered two key parameters in this regard. There are a few studies reporting the corrosion current density ($I_{corr}$) of ALD $Al_2O_3$-protected catalysts. Daubert *et al.* studied the corrosion properties of copper metal protected with different ALD oxide films,[89] whereas another study by Gong *et al.* reported an ALD-$Al_2O_3$ protection scheme on wrought and additively manufactured (AM) stainless steel (SS) 316L.[90] We have converted the $I_{corr}$ values reported in these studies to corrosion rates using eqn (1), and summarized their corrosion properties in Table 1.

$$\text{Corrosion rate} = \frac{I_{corr}A}{nFd} \quad (1)$$

Here, $A$ = atomic weight, $n$ = number of valence electrons, $F$ = Faradaic constant, and $d$ = density.

It can be observed from Table 1 that the dynamic $Al_2O_3$-protected RhCrCo/InGaN in this work has a similar order of magnitude of corrosion rate, and an identical % reduction in corrosion compared to the best ALD $Al_2O_3$-protected catalyst samples.

On the other hand, cocatalyst detachment or leaching is another important photocatalytic stability metric. While this can be suppressed by applying a protective layer on the photocatalyst, it also depends on the nature of the cocatalyst nanoparticle. Lee *et al.* reported ~90% reduction in Co cocatalyst leaching with an ALD $TiO_2$ protection on the Co/$TiO_2$ catalyst.[91] In another study by Settle *et al.*, up to ~96% reduction in Pd cocatalyst leaching has been reported for an ALD $Al_2O_3$-coated Pd/$TiO_2$ catalyst.[92] In this study, with the dynamic $Al_2O_3$ protection, we observe ~93% and ~40% reduction of Rh and Cr cocatalyst detachment, respectively (ESI Fig. S10†).

Table 1 Quantitative comparison of corrosion properties between ALD $Al_2O_3$-protected and dynamic $Al_2O_3$-protected catalyst materials

| Catalyst material | Corrosion rate (nm $h^{-1}$) | Corrosion reduction compared to the unprotected sample | Ref. |
|---|---|---|---|
| 29 nm ALD $Al_2O_3$–Cu | 2.198 | 35.2% | 89 |
| 20 nm ALD $Al_2O_3$-wrought SS316L | 0.066 | 2.6% | 90 |
| 20 nm ALD $Al_2O_3$-AM SS316L | 0.027 | 53.8% | 90 |
| 20 nm dynamic $Al_2O_3$–RhCrCo/InGaN | 0.06 | 66.4% | This work |

Therefore, the dynamic $Al_2O_3$ protection scheme shows mostly identical stability metrics compared to the conventional ALD $Al_2O_3$ protection, while not having the drawback of efficiency degradation. This is because the dynamic $Al_2O_3$ layer can selectively protect the more susceptible *c*-plane of the nanowire photocatalyst from corrosion while not blocking the catalytically active sites on the more robust *m*-plane. As such, this protection scheme does not compromise the photocatalytic efficiency in exchange for long-term stability, unlike the nonporous ALD films.

Furthermore, studies on other artificial photosynthesis systems such as photoelectrochemical (PEC) devices also report the use of ALD-deposited thin $Al_2O_3$ films for enhanced stability in PEC $H_2$ generation through surface passivation.[47,93,94] Besides, Xiao *et al.*[95] reported a remarkably long PEC stability of a GaN/Si photocathode resulting from *in situ* oxynitride formation on the GaN nanowire *m*-plane. Their experiments show the dynamic incorporation of O atoms on the *m*-plane of GaN over time to form atomically thin GaON species, analogous to the sidewall Al oxidation to form the $Al_2O_3$ protection layer as discussed in our study. The GaON nanocluster species serve as catalysts that enhance charge carrier kinetics and function efficiently in a long-term PEC reaction without requiring any additional catalyst regeneration. As such, the dynamic $Al_2O_3$ protection architecture investigated in our study can also be potentially employed in PEC reactions in order to achieve further promising results in stability enhancement.

In addition, electrochemical (EC) processes suffer from different degradation mechanisms such as structural reconfiguration of electrode materials, dendrite growths on electrodes due to non-uniform plating/stripping of metal ions, and attack of chemical species on reactive electrodes.[96] All these factors result in poor EC stability. ALD was utilized to apply precise nanoscale coatings of simple insulators (*i.e.*, $Al_2O_3$) onto common EC electrode materials, creating thin and effective protective layers to achieve enhanced EC stability.[97,98] This approach supported the idea of using thin-film synthesis methods, such as ALD, to form thin protective layers on EC electrodes. By introducing this additional protection layer between the electrode and electrolyte, both the chemical and electrochemical interactions between them are minimized, causing EC performance degradation. Generally, an intentional protection layer in an EC system should possess low electronic conductivity and high ionic conductivity, enabling ion transport between the electrolyte and electrode while preventing electron transfer. Additionally, it is beneficial to design the protection layer to suit a specific EC process, in order to prevent undesirable chemical species from reaching the electrode to mitigate electrode degradation. These combined properties present a formidable interfacial engineering problem in the design of an effective protection architecture in EC systems. As such, the dynamic protection architecture presented in our work can be considered a prospective approach to provide a compelling answer to these challenges.

To summarize, in our work, the initially deposited oxide capping layer helps protect the nanowire *c*-plane from the catalytic etching during the reaction. On the other hand, the dynamically redistributed thin oxide layer on the *m*-plane helps stabilize the cocatalyst nanoparticles on the photocatalyst without any sacrifice in the photocatalytic activity, while the remaining oxide layer on the top *c*-plane still protects against corrosion. Therefore, this kind of oxide protection architecture mitigates the major limiting factors of long-term stability such as photocatalyst corrosion, nanoparticle agglomeration, and nanoparticle detachment, and as such leads to a remarkably enhanced longevity of the photocatalyst material.

## Conclusion

In this study, we have identified the primary factors limiting the long-term stability of p-type InGaN nanowire photocatalysts, those being photocatalytic corrosion and cocatalyst nanoparticle displacement. Detailed analysis suggests that these phenomena severely affect the top *c*-plane of the nanowire structure, limiting the achievable photocatalytic stability to ~250 hours under concentrated solar illumination. As such, protecting the nanowire tip with an oxide capping layer can significantly suppress the photocatalyst etching and cocatalyst nanoparticle displacement occurring at the nanowire surface. Consequently, the Al/$Al_2O_3$-capped Rh/$Cr_2O_3$/$CoO_x$-decorated p-InGaN nanowire sample shows a remarkably enhanced photocatalytic stability of ~1500 hours under the same reaction conditions. Further investigation of this architecture reveals the dynamic nature of the Al/$Al_2O_3$ protection layer, where Al gets redistributed from the *c*-plane toward the *m*-plane, followed by oxidation during the reaction, simultaneously resulting in the nanoparticle stabilization on the *m*-plane and the prevention of the *c*-plane corrosion. Therefore, a proper understanding and design of such an effective protection architecture can not only substantially improve the stability of photocatalytic water splitting but also greatly help achieve the long-term stability of other catalytic reactions, such as nitrogen fixation, carbon dioxide reduction, and various electrochemical reactions.

## Data availability

The data that support the findings of this study are available from the corresponding author upon reasonable request.

## Conflicts of interest

Some IP related to this work was licensed to NS Nanotech, Inc. and NX Fuels, Inc., which were co-founded by Z. Mi. The University of Michigan and Mi have a financial interest in these companies.

## Acknowledgements

This work was supported by NX Fuels and the United States Army Research Office Award W911NF2110337. The authors wish to thank Dr Peng Zhou for his help with some of the experiments.

 

## References

1 C. Liu, N. P. Dasgupta and P. Yang, *Chem. Mater.*, 2014, **26**, 415–422.
2 Y. Tachibana, L. Vayssieres and J. R. Durrant, *Nat. Photonics*, 2012, **6**, 511–518.
3 T. Hisatomi and K. Domen, *Nat. Catal.*, 2019, **2**, 387–399.
4 B. A. Pinaud, J. D. Benck, L. C. Seitz, A. J. Forman, Z. Chen, T. G. Deutsch, B. D. James, K. N. Baum, G. N. Baum, d. Shane Ardo, H. Wang, E. Millere and T. F. Jaramillo, *Energy Environ. Sci.*, 2013, **6**, 1983–2002.
5 C. A. Rodriguez, M. A. Modestino, D. Psaltis and C. Moser, *Energy Environ. Sci.*, 2014, **7**, 3828–3835.
6 J. W. Ager, M. R. Shaner, K. A. Walczak, I. D. Sharpae and S. Ardo, *Energy Environ. Sci.*, 2015, **8**, 2811–2824.
7 D. Kang, J. L. Young, H. Lim, W. E. Klein, H. Chen, Y. Xi, B. Gai, T. G. Deutsch and J. Yoon, *Nat. Energy*, 2017, **2**, 17043.
8 O. Khaselev and J. A. Turner, *Science*, 1998, **280**, 425–427.
9 I. A. Navid, S. Vanka, R. A. Awni, Y. Xiao, Z. Song, Y. Yan and Z. Mi, *Appl. Phys. Lett.*, 2021, **118**, 243906.
10 A. Kudo and Y. Miseki, *Chem. Soc. Rev.*, 2009, **38**, 253–278.
11 Y. Goto, T. Hisatomi, Q. Wang, T. Higashi, K. Ishikiriyama, T. Maeda, Y. Sakata, S. Okunaka, H. Tokudome, M. Katayama, S. Akiyama, H. Nishiyama, Y. Inoue, T. Takewaki, T. Setoyama, T. Minegishi, T. Takata, T. Yamada and K. Domen, *Joule*, 2018, **2**, 509–520.
12 X. Guan, F. A. Chowdhury, N. Pant, L. Guo, L. Vayssieres and Z. Mi, *J. Phys. Chem. C*, 2018, **122**, 13797–13802.
13 J. H. Kim, Y. Jo, J. H. Kim, J. Jang, H. J. Kang, Y. H. Lee, D. S. Kim, Y. Jun and J. S. Lee, *ACS Nano*, 2015, 11820–11829.
14 L. Liao, Q. Zhang, Z. Su, Z. Zhao, Y. Wang, Y. Li, X. Lu, D. Wei, G. Feng, Q. Yu, X. Cai, J. Zhao, Z. Ren, H. Fang, F. Robles-Hernandez, S. Baldelli and J. Bao, *Nat. Nanotechnol.*, 2014, **9**, 69–73.
15 C. Liu, J. Tang, H. M. Chen, B. Liu and P. Yang, *Nano Lett.*, 2013, **13**, 2989–2992.
16 W. Liu, L. Cao, W. Cheng, Y. Cao, X. Liu, W. Zhang, X. Mou, L. Jin, X. Zheng, W. Che, Q. Liu, T. Yao and S. Wei, *Angew. Chem., Int. Ed.*, 2017, **56**, 9312–9317.
17 H. Nishiyama, T. Yamada, M. Nakabayashi, Y. Maehara, M. Yamaguchi, Y. Kuromiya, Y. Nagatsuma, H. Tokudome, S. Akiyama, T. Watanabe, R. Narushima, S. Okunaka, N. Shibata, T. Takata, T. Hisatomi and K. Domen, *Nature*, 2021, **598**, 304–307.
18 Q. Wang, T. Hisatomi, Q. Jia, H. Tokudome, M. Zhong, C. Wang, Z. Pan, T. Takata, M. Nakabayashi, N. Shibata, Y. Li, I. D. Sharp, A. Kudo, T. Yamada and K. Domen, *Nat. Mater.*, 2016, **15**, 611–615.
19 Q. Wang, M. Nakabayashi, T. Hisatomi, S. Sun, S. Akiyama, Z. Wang, Z. Pan, X. Xiao, T. Watanabe, T. Yamada, N. Shibata, T. Takata and K. Domen, *Nat. Mater.*, 2019, **18**, 827–832.
20 I. A. Navid, Y. Shen, P. Zhou, J. Schwartz, Y. M. Goh, T. Ma, R. Hovden, T. Norris and Z. Mi, *AIP Adv.*, 2025, **15**, 015024.
21 Q. Hua, D. Shang, W. Zhang, K. Chen, S. Chang, Y. Ma, Z. Jiang, J. Yang and W. Huang, *Langmuir*, 2011, **27**, 665–671.
22 Y. Kwon, A. Soon, H. Hanb and H. Lee, *J. Mater. Chem. A*, 2015, **3**, 156–162.
23 C. Y. Toe, Z. Zheng, H. Wu, J. Scott, R. Amal and Y. Ng, *Angew. Chem., Int. Ed.*, 2018, **57**, 13613–13617.
24 Z. Zheng, B. Huang, Z. Wang, M. Guo, X. Qin, X. Zhang, P. Wang and Y. Dai, *J. Phys. Chem. C*, 2009, **113**, 14448–14453.
25 S. Peng, Y. Jiang, Z. Wang, X. Luo, J. Lu, L. Han and Y. Ding, *Catal. Lett.*, 2020, **150**, 3533–3541.
26 N. Sakamoto, H. Ohtsuka, T. Ikeda, K. Maeda, D. Lu, M. Kanehara, K. Teramura, T. Teranishib and K. Domen, *Nanoscale*, 2009, **1**, 106–109.
27 S. Chu, P. Ou, R. T. Rashid, P. Ghamari, R. Wang, H. N. Tran, S. Zhao, H. Zhang, J. Song and Z. Mi, *iScience*, 2020, **23**, 101390.
28 Y. Akinaga, T. Kawawaki, H. Kameko, Y. Yamazaki, K. Yamazaki, Y. Nakayasu, K. Kato, Y. Tanaka, A. T. Hanindriyo, M. Takagi, T. Shimazaki, M. Tachikawa, A. Yamakata and Y. Negishi, *Adv. Func. Mater.*, 2023, **33**, 2303321.
29 T. Ikeda, A. Xiong, T. Yoshinaga, K. Maeda, K. Domen and T. Teranishi, *J. Phys. Chem. C*, 2013, **117**, 2467–2473.
30 K. Maeda and K. Domen, *Bull. Chem. Soc. Jpn.*, 2016, **89**, 627–648.
31 R. Shen, L. Hao, Q. Chen, Q. Zheng, P. Zhang and X. Li, *Acta Phys.-Chim. Sin.*, 2022, **38**, 2110014.
32 S. Wang, K. Teramura, T. Hisatomi, H. Asakura, K. Domen, S. Hosokawa and T. Tanaka, *Chem. Sci.*, 2021, **12**, 4940–4948.
33 Z. Wang, Y. Luo, T. Hisatomi, J. J. M. Vequizo, S. Suzuki, S. Chen, M. Nakabayashi, L. Lin, Z. Pan, N. Kariya, A. Yamakata, N. Shibata, T. Takata, K. Teshima and K. Domen, *Nat. Commun.*, 2021, **12**, 1005.
34 K. Yoshioka, M. Yamamoto, T. Tanabe and T. Yoshida, *e-J. Surf. Sci. Nanotechnol.*, 2020, **18**, 168–174.
35 H. Lyu, T. Hisatomi, Y. Goto, M. Yoshida, T. Higashi, M. Katayama, T. Takata, T. Minegishi, H. Nishiyama, T. Yamada, Y. Sakata, K. Asakura and K. Domen, *Chem. Sci.*, 2019, **10**, 3196.
36 T. Ohno, L. Bai, T. Hisatomi, K. Maeda and K. Domen, *J. Am. Chem. Soc.*, 2012, **134**, 8254–8259.
37 P. Zhou, I. A. Navid, Y. Ma, Y. Xiao, P. Wang, Z. Ye, B. Zhou, K. Sun and Z. Mi, *Nature*, 2023, **613**, 66–70.
38 X. Chen, S. Shen, L. Guo and S. S. Mao, *Chem. Rev.*, 2010, **110**, 6503–6570.
39 P. G. Moses and C. G. V. d. Walle, *Appl. Phys. Lett.*, 2010, **96**, 021908.
40 J. Wu, *J. Appl. Phys.*, 2009, **106**, 011101.
41 I. A. Navid, Y. Liu, Y. Pan, K. Sun, E. Kioupakis and Z. Mi, *APL Mater.*, 2024, **12**, 021118.
42 I. A. Navid, A. Pandey, Y. M. Goh, J. Schwartz, R. Hovden and Z. Mi, *Adv. Opt. Mater.*, 2022, **10**, 2102263.
43 J. Li, J. Y. Lin and H. X. Jiang, *Appl. Phys. Lett.*, 2008, **93**, 162107.
44 D. Zhuang and J. H. Edgar, *Mater. Sci. Eng., R*, 2005, **48**, 1–46.
45 Y. Kuang, Q. Jia, G. Ma, T. Hisatomi, T. Minegishi, H. Nishiyama, M. Nakabayashi, N. Shibata, T. Yamada, A. Kudo and K. Domen, *Nat. Energy*, 2016, **2**, 16191.

46 S. Vanka, K. Sun, G. Zeng, T. A. Pham, F. M. Toma, T. Ogitsu and Z. Mi, *J. Mater. Chem. A*, 2019, **7**, 27612.
47 S. Vanka, B. Zhou, R. A. Awni, Z. Song, F. A. Chowdhury, X. Liu, H. Hajibabaei, W. Shi, Y. Xiao, I. A. Navid, A. Pandey, R. Chen, G. A. Botton, T. W. Hamann, D. Wang, Y. Yan and Z. Mi, *ACS Energy Lett.*, 2020, **5**, 3741–3751.
48 Z. Yin, R. Fan, G. Huang and M. Shen, *Chem. Commun.*, 2018, **54**, 543–546.
49 J. L. Young, M. A. Steiner, H. Döscher, R. M. France, J. A. Turner and T. G. Deutsch, *Nat. Energy*, 2017, **2**, 17028.
50 K. Han, D. M. Haiber, J. Knöppel, C. Lievens, S. Cherevko, P. Crozier, G. Mul and B. Mei, *ACS Catal.*, 2021, **11**, 11049–11058.
51 M. G. Kibria, F. A. Chowdhury, S. Zhao, B. AlOtaibi, M. L. Trudeau, H. Guo and Z. Mi, *Nat. Commun.*, 2015, **6**, 6797.
52 G. Dong, H. Hu, X. Huang, Y. Zhanga and Y. Bi, *J. Mater. Chem. A*, 2018, **6**, 21003–21009.
53 M. Liu, G. Zhang, X. Liang, Z. Pan, D. Zheng, S. Wang, Z. Yu, Y. Hou and X. Wang, *Angew. Chem., Int. Ed.*, 2023, **62**, e202304694.
54 K. Maeda, K. Teramura, D. Lu, N. Saito, Y. Inoue and K. Domen, *J. Phys. Chem. C*, 2007, **111**, 7554–7560.
55 H. Sudrajat, S. Babel, S. Hartuti, J. Phanthuwongpakdee, K. Laohhasurayotin, T. K. Nguyen and H. D. Tong, *Int. J. Hydrogen Energy*, 2021, **46**, 31228–31238.
56 Q. Zhang, Y. Xiao, Y. Li, K. Zhao, H. Deng, Y. Lou, J. Chen, H. Yu and L. Cheng, *Chem. Eng. J.*, 2020, **393**, 124681.
57 Y. Xiao, S. Vanka, T. A. Pham, W. J. Dong, Y. Sun, X. Liu, I. A. Navid, J. B. Varley, H. Hajibabaei, T. W. Hamann, T. Ogitsu and Z. Mi, *Nano Lett.*, 2022, **22**, 2236–2243.
58 G. W. Busser, B. Mei, P. Weide, P. C. K. Vesborg, K. Stührenberg, M. Bauer, X. Huang, M.-G. Willinger, I. Chorkendorff, R. Schlögl and M. Muhler, *ACS Catal.*, 2015, **5**, 5530–5539.
59 J. Gu, Y. Yan, J. W. Krizan, Q. D. Gibson, Z. M. Detweiler, R. J. Cava and A. B. Bocarsly, *J. Am. Chem. Soc.*, 2014, **136**, 830–833.
60 U. Ulmer, T. Dingle, P. N. Duchesne, R. H. Morris, A. Tavasoli, T. Wood and G. A. Ozin, *Nat. Commun.*, 2019, **10**, 3169.
61 F. Leroy, A. E. Barraj, F. Cheynis, P. Müller and S. Curiotto, *Phys. Rev. Lett.*, 2023, **131**, 116202.
62 H. B. HUNTINGTON, *J. Phys. Chem. Solids*, 1968, **29**, 1641–1651.
63 G. Zhao, E. Jeong, S.-G. Lee, J.-S. Bae, S. M. Yu, S. Z. Han, G.-H. Lee, E.-A. Choi and J. Yun, *Appl. Surf. Sci.*, 2022, **588**, 152907.
64 S. Kundu, A. Pal and A. K. Dikshit, *Sep. Purif. Technol.*, 2005, **44**, 121–129.
65 L. Sánchez, J. peral and X. Domènech, *Electrochim. Acta*, 1996, **41**(13), 1981–1985.
66 H. Wu and J. Zhang, *Chem. Commun.*, 2025, **61**, 2190–2202.
67 H. Zhang, L. Chen, F. Dong, Z. Lu, E. Lv, X. Dong, H. Li, Z. Yuan, X. Peng, S. Yang, J. Qiu, Z. Guo and Z. Wen, *Energy Environ. Sci.*, 2024, **17**, 6435–6481.
68 P. Paciok, M. Schalenbach, M. Carmo and D. Stolten, *J. Power Sources*, 2017, **365**, 53–60.
69 W. J. Dong, Z. Ye, S. Tang, I. A. Navid, Y. Xiao, B. Zhang, Y. Pan and Z. Mi, *Adv. Sci.*, 2024, **1–9**, 2309548.
70 Y. Wang, T. L. Alford and J. W. Mayer, *J. Appl. Phys.*, 1999, **86**(10), 5407–5412.
71 G. Botzolaki, G. Goula, A. Rontogianni, E. Nikolaraki, N. Chalmpes, P. Zygouri, M. Karakassides, D. Gournis, N. Charisiou, M. Goula, S. Papadopoulos and I. Yentekakis, *Catalysts*, 2020, **10**, 941.
72 G. Goula, G. Botzolaki, A. Osatiashtiani, C. M. A. Parlett, G. Kyriakou, R. M. Lambert and I. V. Yentekakis, *Catalysts*, 2019, **9**, 541.
73 J. A. Moulijn, A. E. v. Diepen and F. Kapteijn, *Appl. Catal., A*, 2001, **212**, 3–16.
74 M. D. Argyle and C. H. Bartholomew, *Catalysts*, 2015, **5**, 145–269.
75 A. Datye and Y. Wang, *Natl. Sci. Rev.*, 2018, **5**(5), 630–632.
76 J. Jones, H. Xiong, A. T. DeLaRiva, E. J. Peterson, H. Pham, S. R. Challa, G. Qi, S. Oh, M. H. Wiebenga, X. I. P. Hernández, Y. Wang and A. K. Datye, *Science*, 2016, **353**(6295), 150–154.
77 F. C. Richard and A. C. M. Bourg, *Water. Res.*, 1991, **25**(7), 807–816.
78 W. Wei, B. Zhang, L. Zhang and X. Yu, *ECS J. Solid State Sci. Technol.*, 2022, **11**, 034002.
79 S. Zhang, A. T. Connie, D. A. Laleyan, H. P. T. Nguyen, Q. Wang, J. Song, I. Shih and Z. Mi, *IEEE J. Quantum Electron.*, 2014, **50**, 483–490.
80 A. Kanevce, D. H. Levi and D. Kuciauskas, *Prog. Photovoltaics Res. Appl.*, 2014, **22**, 1138–1146.
81 Y.-C. Pu, M. G. Kibria, Z. Mi and J. Z. Zhang, *J. Phys. Chem. Lett.*, 2015, **6**, 2649–2656.
82 Y. Zhao, L. Xie, H. Chen, X. Wang, Y. Chen, G. Zhou and R. Nötzel, *Front. Phys.*, 2021, **9**, 684283.
83 L. Yang, M. Lv, Y. Song, K. Yin, X. Wang, X. Cheng, K. Cao, S. Li, C. Wang, Y. Yao, W. Luo and Z. Zou, *Appl. Catal., B*, 2020, **279**, 119341.
84 H. Yi, H. Du, Y. Hu, H. Yan, H.-L. Jiang and J. Lu, *ACS Catal.*, 2015, **5**, 2735–2739.
85 Z. Li, F. Hong, R. Li, N. Ta, H. Jing, X. Zhang, J. Xiao, J. Zhu, H. Xie and C. Li, *Nat. Catal.*, 2022, **6**, 80–88.
86 A. C. Alba-Rubio, B. J. O'Neill, F. Shi, C. Akatay, C. Canlas, T. Li, R. Winans, J. W. Elam, E. A. Stach, P. M. Voyles and J. A. Dumesic, *ACS Catal.*, 2014, **4**, 1554–1557.
87 J. Lee, D. H. K. Jackson, T. Li, R. E. Winans, J. A. Dumesic, T. F. Kuech and G. W. Huber, *Energy Environ. Sci.*, 2014, **7**, 1657.
88 M. Liu, X. Bao, F. Ma, M. Wang, L. Zheng, Z. Wang, P. Wang, Y. Liu, H. Cheng, Y. Dai, Y. Fan, Z. Zheng and B. Huang, *J. Chem. Eng.*, 2022, **429**, 132022.
89 J. S. Daubert, G. T. Hill, H. N. Gotsch, A. P. Gremaud, J. S. Ovental, P. S. Williams, C. J. Oldham and G. N. Parsons, *ACS Appl. Mater. Interfaces*, 2017, **9**, 4192–4201.

 

90 N. Gong, H. Seet, J. Cao, T. L. Meng, Y. Wang, D. C. C. Tan, C. K. I. Tan, A. Suwardi, Q. Zhu, D. J. Blackwood, M. L. S. Nai and H. Liu, *Mater. Lett.*, 2023, **331**, 133434.
91 J. Lee, D. H. K. Jackson, T. Li, R. E. Winans, J. A. Dumesic, T. F. Kuech and G. W. Huber, *Energy Environ. Sci.*, 2014, **7**, 1657–1660.
92 A. E. Settle, N. S. Cleveland, C. A. Farberow, D. R. Conklin, X. Huo, A. A. Dameron, R. W. Tracy, R. Sarkar, E. J. Kautz, A. Devaraj, K. K. Ramasamy, M. J. Watson, A. M. York, R. M. Richards, K. A. Unocic, G. T. Beckham, M. B. Griffin, K. E. Hurst, E. C. D. Tan, S. T. Christensen and D. R. Vardon, *Joule*, 2019, **3**, 2219–2240.
93 R. Fan, W. Dong, L. Fang, F. Zheng, X. Su, S. Zou, J. Huang, X. Wang and M. Shen, *Appl. Phys. Lett.*, 2015, **106**, 013902.
94 M. J. Choi, J.-Y. Jung, M.-J. Park, J.-W. Song, J.-H. Lee and J. H. Bang, *J. Mater. Chem. A*, 2014, **2**, 2928.
95 Y. Xiao, X. Kong, S. Vanka, W. J. Dong, G. Zeng, Z. Ye, K. Sun, I. A. Navid, B. Zhou, F. Toma, H. Guo and Z. Mi, *Nat. Commun.*, 2023, **14**, 2047.
96 C.-F. Lin, Y. Qi, K. Gregorczyk, S. B. Lee and G. W. Rubloff, *Acc. Chem. Res.*, 2018, **51**, 97–106.
97 L. A. Riley, A. S. Cavanagh, S. M. George, Y. S. Jung, Y. Yan, S.-H. Lee and A. C. Dillon, *ChemPhysChem*, 2010, **11**, 2124–2130.
98 Y. S. Jung, A. S. Cavanagh, L. A. Riley, S.-H. Kang, A. C. Dillon, M. D. Groner, S. M. George and S.-H. Lee, *Adv. Mater.*, 2010, **22**, 2172–2176.